

RESEARCH ARTICLE | MAY 02 2024

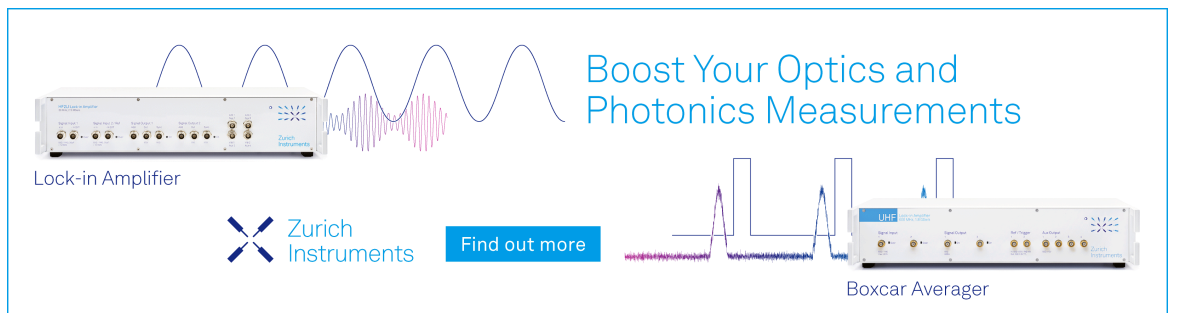
Status of h-BN quasi-bulk crystals and high efficiency neutron detectors

Special Collection: [Native Defects, Impurities and the Electronic Structure of Compound Semiconductors: A Tribute to Dr. Wladyslaw Walukiewicz](#)

Z. Alemous  ; A. Tingsuwatit  ; A. Maity  ; J. Li  ; J. Y. Lin   ; H. X. Jiang  

 Check for updates

J. Appl. Phys. 135, 175704 (2024)
<https://doi.org/10.1063/5.0179610>



Boost Your Optics and Photonics Measurements

Lock-in Amplifier

 Zurich Instruments

[Find out more](#)

Boxcar Averager

Status of h-BN quasi-bulk crystals and high efficiency neutron detectors

Cite as: J. Appl. Phys. 135, 175704 (2024); doi: 10.1063/5.0179610

Submitted: 3 October 2023 · Accepted: 19 April 2024 ·

Published Online: 2 May 2024



Z. Alemoush, A. Tingsuwatit, A. Maity, J. Li, J. Y. Lin,^{a)} and H. X. Jiang^{a)}

AFFILIATIONS

Department of Electrical and Computer Engineering, Texas Tech University, Lubbock, Texas 79409, USA

Note: This paper is part of the Special Topic on Native Defects, Impurities and the Electronic Structure of Compound Semiconductors: A Tribute to Dr. Wladyslaw Walukiewicz.

^{a)}Authors to whom correspondence should be addressed: hx.jiang@ttu.edu and jingyu.lin@ttu.edu

ABSTRACT

III-nitrides have fomented a revolution in the lighting industry and are poised to make a huge impact in the field of power electronics. In the III-nitride family, the crystal growth and use of hexagonal BN (h-BN) as an ultrawide bandgap (UWBG) semiconductor are much less developed. Bulk crystals of h-BN produced by the high-temperature/high-pressure and the metal flux solution methods possess very high crystalline and optical qualities but are impractical to serve as substrates or for device implementation as their sizes are typically in millimeters. The development of crystal growth technologies for producing thick epitaxial films (or quasi-bulk or semi-bulk crystals) in large wafer sizes with high crystalline quality is a prerequisite for utilizing h-BN as an UWBG electronic material. Compared to traditional III-nitrides, BN has another unique application as solid-state neutron detectors, which however, also require the development of quasi-bulk crystals to provide high detection efficiencies because the theoretical efficiency (η_i) relates to the detector thickness (d) by $\eta_i = 1 - e^{-d/\lambda}$, where λ denotes the thermal neutron absorption length which is $47\ \mu\text{m}$ ($237\ \mu\text{m}$) for ^{10}B -enriched (natural) h-BN. We provide an overview and recent progress toward the development of h-BN quasi-bulk crystals via hydride vapor phase epitaxy (HVPE) growth and the attainment of thermal neutron detectors based on $100\ \mu\text{m}$ thick ^{10}B -enriched h-BN with a record efficiency of 60%. The thermal neutron detection efficiency was shown to enhance at elevated temperatures. Benchmarking the crystalline and optical qualities of h-BN quasi-bulk crystals with the state-of-the-art mm-sized bulk crystal flakes and $0.5\ \mu\text{m}$ thick epitaxial films identified that reducing the density of native defects such as vacancies remains the most critical task for h-BN quasi-bulk crystal growth by HVPE.

© 2024 Author(s). All article content, except where otherwise noted, is licensed under a Creative Commons Attribution-NonCommercial 4.0 International (CC BY-NC) license (<https://creativecommons.org/licenses/by-nc/4.0/>). <https://doi.org/10.1063/5.0179610>

I. INTRODUCTION

III-nitride wide bandgap (WBG) semiconductors have revolutionized the lighting and consumer electronics industries.^{1–3} InGaN alloys are also making inroads in full-spectrum solar cell and full color display applications, in part attributed to the pioneering experimental work by Wu *et al.* that pinned down the bandgap of InN to be $\sim 0.7\ \text{eV}$.⁴ Today, ultrawide bandgap semiconductors (UWBGs) have also garnered significant attention for power electronic and deep UV (DUV) photonic devices.^{5,6} The potential of UWBGs for THz and sub-THz applications is also being evaluated.⁷ These recent developments are due to the superior intrinsic physical properties of UWBGs. As a member of the III-nitride family, with its bandgap at about 6 eV, the crystal growth and use

of hexagonal BN (h-BN) as an UWBGs are much less developed.^{8–11} Instead, h-BN in its two-dimensional (2D) form, consisting of one or a few-layers of h-BN, has been extensively investigated as a complementary dielectric substrate and gate material for 2D and graphene materials.^{12–14} More recently, optically stable single photon emitters have also been observed in 2D h-BN,^{15–18} opening the potential of 2D h-BN as a qubit device material.

Bulk crystals of h-BN produced by the high-temperature/high-pressure (HT/HP)^{9,10,19–21} and the metal flux solution method^{22,23} possess very high crystalline and optical qualities but remain at millimeter in size, rendering them impractical as substrates or for device implementation. The development of crystal growth technologies for producing epitaxial films in 10 s to 100 s of microns in

02 May 2024 20:44:59

thickness (or quasi-bulk crystals) in large wafer sizes is prerequisite for utilizing the full potential of h-BN for device applications. Here, we provide a brief overview on the recent progress toward the synthesizing of h-BN quasi-bulk crystals by hydride vapor phase epitaxy (HVPE) and the realization of high efficiency thermal neutron detectors based on ^{10}B -enriched h-BN (h- ^{10}B N) achieved exclusively by our group. The understanding of the dominant defects that limit the performance of h-BN devices is also discussed.

II. EXPERIMENT, RESULTS, AND DISCUSSION

A. Benchmarking crystalline and optical qualities

To produce h-BN quasi-bulk wafers, HVPE growth is adopted, which is a proven epitaxial growth technique capable of producing high-quality GaN and AlN quasi-bulk wafers at high growth rates, up to 100 s of microns per hour.^{24–26} More recently, it was also demonstrated that HVPE growth technique is capable to produce GaN with significantly reduced background impurity concentrations²⁷ and improved p-type conductivity²⁸ over those produced by metal organic chemical vapor deposition (MOCVD) because precursors for HVPE growth are free from carbon impurities.

To grow h-BN wafers by HVPE, boron trichloride (BCl_3) and NH_3 were used as precursors and hydrogen was used as a carrier gas. The growth was conducted on *c*-plane sapphire of 2-in. or 4-in. in diameter at a growth temperature of around 1500 °C.^{29,30} As illustrated in Fig. 1(a), h-BN is the only material among III-nitrides to possess a layered crystalline structure with a bulk *a*-lattice constant of 0.250 nm and *c*-lattice constant of 0.666 nm.³¹ Because of its unique crystalline structure, a h-BN wafer tends to self-separate from sapphire to form a freestanding wafer during

cooling down after growth when the thickness is exceeding $\sim 10\ \mu\text{m}$ ²⁹ and this exclusive feature is illustrated in Fig. 1(b). The thickest HVPE h-BN quasi-bulk wafers produced by our group as of this writing has a thickness of $\sim 500\ \mu\text{m}$, as probed by a thickness profilometer. An example of thickness calibration is shown in Fig. 1(c).

Bulk h-BN single crystals produced by the high-temperature/high-pressure (HT/HP)^{9,10,19–21} or by the metal flux solution method at atmospheric pressures^{22,23} possess the highest crystalline and optical qualities. On the other hand, MOCVD is a highly established epitaxial growth technique for producing III-nitride thin epitaxial film (or epilayer) wafers as well as device structures with an excellent overall material quality. We are among the various groups that have successfully demonstrated MOCVD growth of high-quality epitaxial layers of h-BN with a thickness ranging from a few layers to a few microns^{32–38} and demonstrated the ability of h-BN for neutron sensing.^{33–36} Therefore, benchmarking the overall crystalline and optical qualities of h-BN quasi-bulk crystals produced by HVPE against those of the state-of-the-art mm-sized bulk crystals and MOCVD grown thin epilayers provides valuable insights regarding how much room is there as well as key areas for further improvement.

In Fig. 2, we compare the x-ray diffraction patterns (in XRD 2θ - ω scans) of h-BN crystals synthesized by the metal flux solution method,²² a $0.5\ \mu\text{m}$ thick h-BN epilayer produced by MOCVD, and a $100\ \mu\text{m}$ thick freestanding h-BN quasi-bulk wafer produced by HVPE. The $0.5\ \mu\text{m}$ thick h-BN epilayer was grown by MOCVD on *c*-plane sapphire substrate using a pulsed precursor flow growth scheme (alternating flows of triethylboron and NH_3) developed previously.³⁸ For the h-BN bulk flake, MOCVD thin epilayer, and HVPE quasi-bulk samples, the XRD peak corresponding to diffraction by the h-BN (002) plane (stacked planes in

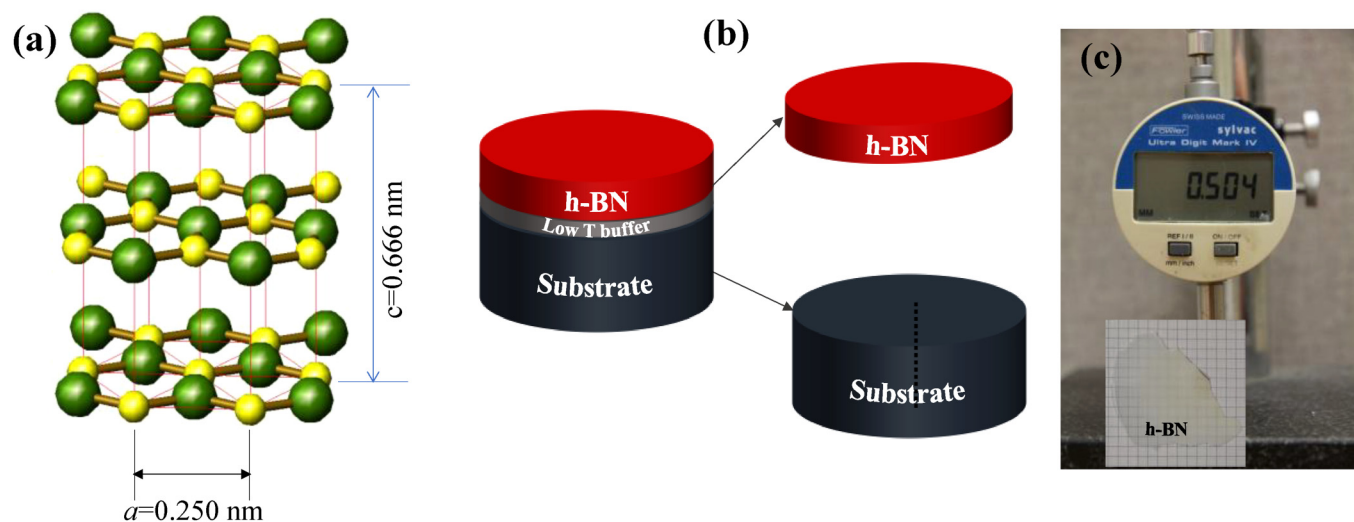


FIG. 1. (a) Schematic of the crystalline structure of h-BN, illustrating its layered structure. (b) Schematic for obtaining freestanding h-BN quasi-bulk wafers via self-separation during cooling down after growth due to its layered structure. (c) Demonstration of our recent attainment of a h-BN quasi-bulk wafer with a thickness of about $500\ \mu\text{m}$.

02 May 2024 20:44:59

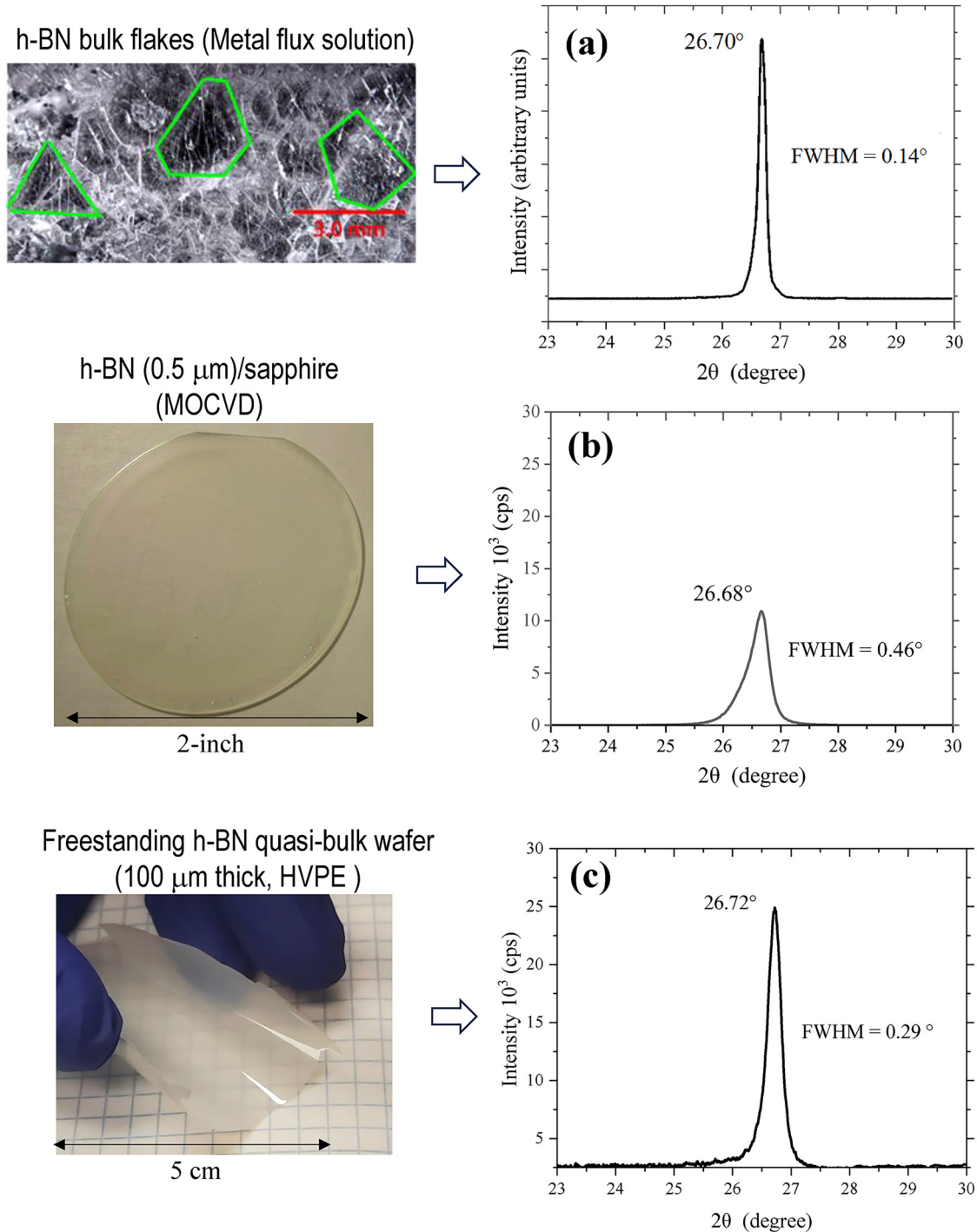


FIG. 2. Comparison of micrographs and x-ray diffraction patterns in 2θ - ω scans: (a) a bulk crystal flake synthesized by the metal flux solution method at atmospheric pressures [figure reproduced from Figs. 1(c) and 2(d) of Ref. 22 with permission from Li *et al.*, Chem. Mater. **32**, 5066 (2020). Copyright 2020 American Chemical Society]. (b) A h-BN (0.5 μm)/sapphire epilayer synthesized by MOCVD using a pulsed precursor flow scheme. (c) A 100 μm thick freestanding flexible h-BN quasi-bulk wafer synthesized by HVPE.

the *c*-direction) is centered at $2\theta = 26.70^\circ$, 26.68° , and 26.72° , respectively. Since the *c*-lattice constant of a perfect h-BN bulk crystal is 0.666 nm, corresponding to a diffraction peak of the h-BN (002) plane at $2\theta = 26.74^\circ$,³¹ the measured XRD peak positions imply that the HVPE grown quasi-bulk crystal has a *c*-lattice constant closest to the ideal $c = 0.666$ nm among these three samples compared. On the other hand, the bulk crystal flake exhibits the narrowest full width at the half maximum (FWHM) of 0.14° . HVPE quasi-bulk wafer has a FWHM of 0.29° and the $0.5\ \mu\text{m}$ thick epilayer has a FWHM of 0.46° .

XRD 2θ - ω scans in a large angle range with an open detector are also compared in Fig. 3 for the three types of materials. Diffraction peaks from h-BN (002), (004), and (006) planes were clearly observable in both the bulk crystal synthesized by the HT/HP method²¹ and the freestanding h-BN quasi-bulk wafer [Figs. 3(a) and 3(c)], revealing the same peak positions in both samples and meaning that both type of samples have a very good long-range order in the *c*-axis. However, the XRD linewidths of the diffraction peaks are broader in h-BN quasi-bulk wafer than those in the bulk crystal produced by the HP/HT method.²¹ For the $0.5\ \mu\text{m}$ thick epilayer on sapphire, diffraction peaks from the h-BN (002), h-BN (004), and sapphire (006) planes are clearly observable, while from the h-BN (006) plane was hardly visible, possibly related to the small thickness of the film. The comparison results shown in Figs. 2 and 3 indicate that our h-BN quasi-bulk wafers produced by HVPE have a good stacking sequence and long-range order in the *c* axis.

However, the FWHM of the XRD diffraction (XRD) peak is narrowest for HT/HP bulk crystals, which implies that bulk crystals have the best structural ordering in the *c*-plane. It is worth to pointing out that the h-BN (002) peak of the $500\ \mu\text{m}$ thick wafer (not shown) appears at a lower diffraction angle in comparison with $2\theta = 26.72^\circ$ observed in the $100\ \mu\text{m}$ thick wafer, indicating that the stacking sequence in the *c*-direction deteriorates with increasing wafer thickness and there is a lot of room for further improvement.

Next, we compare the optical properties by measuring their photoluminescence (PL) emission spectra. The excitation source was a frequency quadrupled Ti:sapphire laser with an excitation photon wavelength set at 195 nm and a monochromator (1.3 m) in conjunction with a photomultiplier tube (PMT) was used to disperse and record PL spectra. In the PL spectrum of the bulk crystal shown in Fig. 4(a),²³ six sharp emission lines were resolved between 5.75 and 5.90 eV, which have been attributed to the intrinsic or free-exciton (FX) transitions and labeled as S-series lines.^{23,39} The observation of the FX transitions implies that the bulk crystal produced by the metal flux solution method has a relatively low density of defects.

The h-BN epilayer/sapphire shown in Fig. 4(b) exhibits a dominant emission peak at 5.735 eV, which is most likely also associated with exciton transition in h-BN thin epilayers produced by MOCVD using a pulsed flow growth scheme.³⁸ One additional peak around 5.58 eV may be due to impurity related transition. As previously discussed, the candidates of impurities and defects involved in MOCVD grown epilayers include carbon impurities which are from the MOCVD boron precursor and nitrogen vacancies. Oxygen is another hard to avoid impurity because the

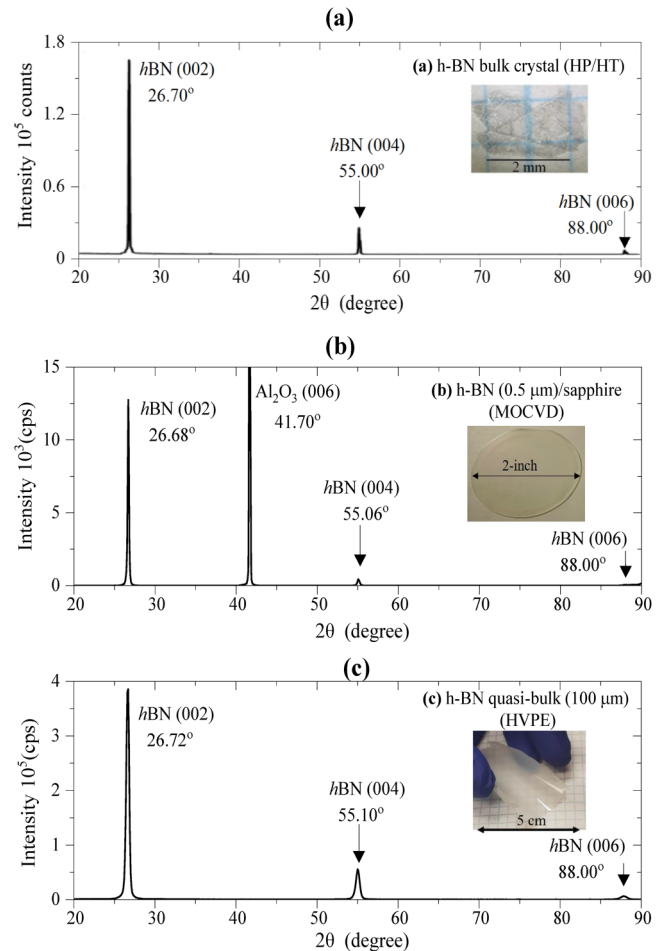


FIG. 3. Comparison of x-ray diffraction (XRD) patterns in 2θ - ω scans in a large angle range with an open detector: (a) A bulk crystal flake synthesized by the high-temperature/high-pressure (HT/HP) method [figure reproduced from Fig. 4 of Ref. 21 with permission from Zhigadlo, *J. Cryst. Growth* **402**, 308 (2014). Copyright Elsevier; License No. 5638910313245]. (b) A h-BN ($0.5\ \mu\text{m}$)/sapphire epilayer synthesized by MOCVD using a pulsed flow growth scheme. (c) A $100\ \mu\text{m}$ thick freestanding flexible h-BN quasi-bulk wafer synthesized by HVPE.

epilayers are deposited on sapphire substrates.⁴⁰ Nonetheless, the PL spectrum of this thin epilayer clearly exhibits a weaker emission peak near 5.95 eV. In comparison, as shown in Fig. 4(c), HVPE grown quasi-bulk wafer exhibits a dominant emission line near 3.6 eV regardless of the measurement temperatures, which was attributed to a donor-acceptor pair (DAP) recombination,^{30,41} involving possibly oxygen donors (O_N) and boron vacancy – hydrogen complex deep level acceptors.⁴² A band-edge emission peak near 5.9 eV, which is $\sim 100\times$ weaker than the impurity emission line, is also observable. The comparison results of PL emission spectra point out that optimizing the growth conditions to reduce the density of native defects such as vacancies and residue impurities such as oxygen is the most critical task for the further

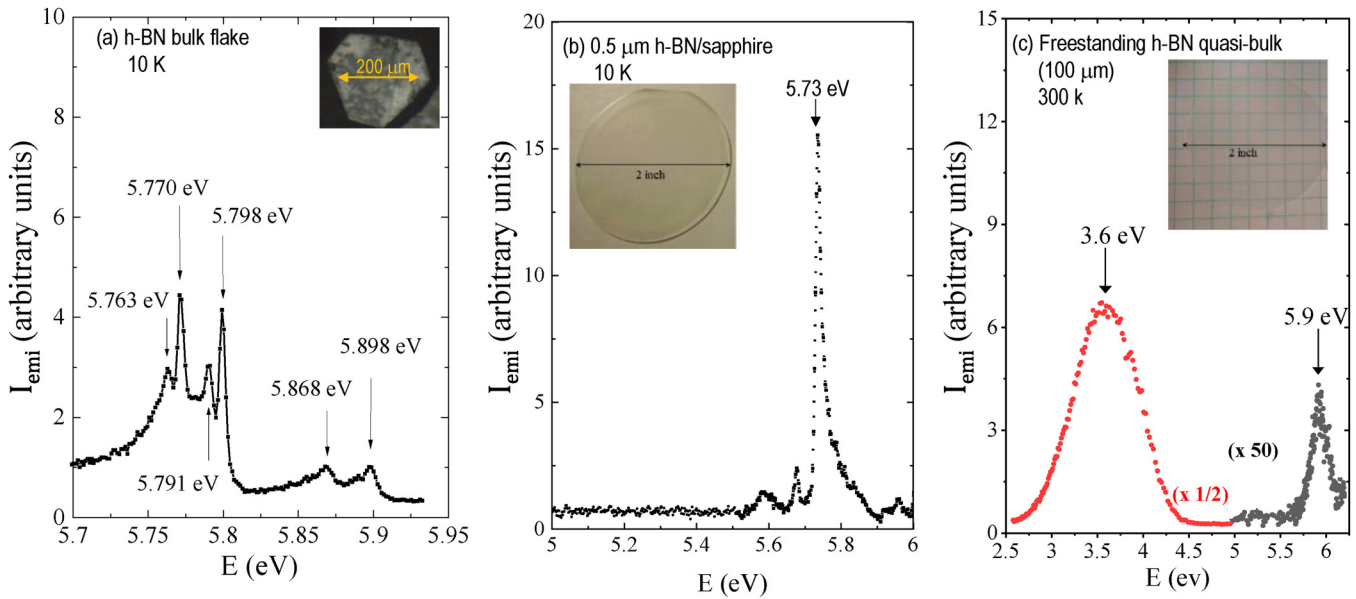


FIG. 4. Comparison of photoluminescence (PL) emission spectra: (a) a bulk crystal flake synthesized by the metal flux solution method at atmospheric pressures [figure reproduced from Fig. 2(b) of Ref. 23, Li *et al.*, Appl. Phys. Lett. **108**, 122101 (2016). Copyright 2016 AIP Publishing LLC]. (b) A h-BN (0.5 μm)/sapphire epilayer synthesized by MOCVD using a pulsed growth scheme. (c) A 100 μm thick freestanding h-BN quasi-bulk wafer synthesized by HVPE [figure reproduced from Fig. 2(b) of Ref. 41, Almomhammad *et al.*, Appl. Phys. Lett. **124**, 102106 (2024). Copyright 2024 AIP Publishing LLC].

advancement of h-BN quasi-bulk crystal growth by HVPE. Boron vacancy complex centers are predicted to have a dominant charge state of (0/−1) with low formation energy,⁴² which can function as carrier traps and are expected to have a detrimental effect on the device performance.

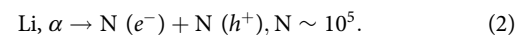
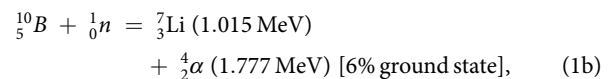
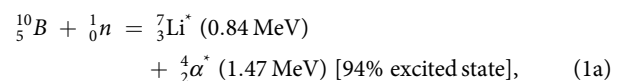
On the other hand, we believe that this is the first observation of the band-edge emission lines near 5.9 eV in wafers produced by epitaxial growth techniques of MOCVD and HVPE. The PL spectra shown in Figs. 4(b) and 4(c) indicate that both of our thin epitaxial layers and quasi-bulk crystal wafers have a decent crystalline quality, and the PL results corroborate with the XRD results shown in Figs. 2 and 3. The observation of the emission lines near the bandgap of h-BN provides new opportunities for probing and understanding the detailed band structures of h-BN.

In a similar scenario in the development history of III-nitrides, eliminating (or minimizing) native defects will be necessary prior to the development of h-BN doping and h-BN based devices. However, as we will discuss in the next sections, simple photo-conductive type of detectors fabricated from 100 μm thick ¹⁰B-enriched h-BN quasi-bulk crystals have attained a record high detection efficiency for thermal neutrons. These devices offer advantages of compact size, high gamma rejection ratio, low voltage operation, radiation hardness, capabilities for operating at elevated temperatures⁴³ and in harsh environments and ability for detecting thermal and fast neutrons simultaneously.⁴⁴ Moreover, the development of high efficiency h-BN neutron detector technology also serves as a stepstone for advancing the crystal growth technology to produce electronic grade h-BN quasi-bulk wafers, which

will ultimately open the door for utilizing h-BN as an UWBG electronic material.

B. Principle of h-BN direct conversion thermal neutron detectors

BN sets itself apart from other III-nitride semiconductors by the fact that the isotope ¹⁰B possesses a large cross section of ~3840 barns (=3.84 × 10^{−21} cm²) for thermal neutrons (σ).^{45,46} Element B exists in two main isotopes, ¹⁰B and ¹¹B in a natural abundance of approximately 20% and 80%, respectively. It is only the isotope ¹⁰B that can interact effectively with thermal neutrons. The operating principle of BN neutron detectors is based on the absorption of a neutron by a ¹⁰B atom, which induces the following nuclear reaction inside h-BN:⁴⁶



The detection of thermal neutrons by a h-BN detector is accomplished by a three-step process: (a) the first is the neutron

absorption of Eq. (1) in which the nuclear reaction creates Li and α daughter particles with large kinetic energies; (2) the second process of Eq. (2) is the subsequent charge carrier [electrons (e^-) and holes (h^+)] generation by Li and α particles; and (3) the final process of the charge carrier (electrons and holes) separation and collection by the electrodes with the aid of an applied bias voltage or electric field.

As shown in Fig. 5(a), ^{10}B has a thermal neutron cross section (σ) of $3.84 \times 10^{-21} \text{ cm}^2$ (for neutrons with an average kinetic energy of 25 meV).^{45,46} As a semiconductor, the density of B atoms (N) which can interact with thermal neutrons in 100% ^{10}B -enriched BN is $5.5 \times 10^{22}/\text{cm}^3$. This provides a thermal neutron macroscopic absorption coefficient (α) of 211.2 per cm and a thermal neutron absorption length (λ) of $47.3 \mu\text{m}$ in h- ^{10}B N (5 \times larger or $237 \mu\text{m}$ in natural h-BN), where α and λ are obtained from the relations of $\alpha = N\sigma = 5.5 \times 10^{22} \times 3.84 \times 10^{-21} = 211.2 \text{ cm}^{-1}$ and $\lambda = \alpha^{-1}$.

The intrinsic detection efficiency (η_i) of neutron detectors as a function of the detector's layer thickness, d , can be described by the standard absorption equation,

$$\eta_i = 1 - e^{-d/\lambda} \quad (3)$$

where d denotes the detector thickness and λ the thermal neutron absorption length. Equation (3) is plotted in Fig. 5(b), which shows that the intrinsic efficiency can be increased by increasing the h-BN layer thickness and h- ^{10}B N (h-BN) wafers with a layer thickness $d > \lambda$ of $47.3 \mu\text{m}$ ($237 \mu\text{m}$) are needed to achieve thermal neutron detectors with an intrinsic detection efficiency (or neutron absorption) exceeding 63% ($=1 - e^{-1}$).

C. h-BN neutron detector fabrication and efficiency measurements

Based on Eq. (3), obtaining h-BN wafers with a large thickness is necessary to ensure a high intrinsic detection efficiency. On the other hand, achieving a high charge collection efficiency is also necessary to ensure an overall high detection efficiency. The most important parameters for determining the charge collection efficiency of a neutron detector are its carrier mobility and lifetime product, $\mu_i \tau_i$, and surface recombination field, s_i/μ_i . Here, i denotes electron (e) or hole (h) and s_i denotes the surface recombination velocity, which is determined by the density of defects and impurities that can trap radiation-generated charge carriers. To the first order, the first condition for charge collection is that the charge carrier drift length, $E_a \mu_i \tau_i$, must be greater than the transit length, ℓ ,

$$(a) \quad \frac{\ell}{E_a \mu_i \tau_i} = \frac{\ell^2}{V \mu_i \tau_i} \ll 1, \quad (4a)$$

where ℓ is the spacing between the two electrodes. For vertical detectors, ℓ is the device thickness, $\ell = d$. For lateral devices, ℓ is the detector's width, $\ell = W$. The second condition for charge collection is that the applied electric field, V/ℓ , must be greater than the surface recombination field, s_i/μ_i ,

$$(b) \quad \frac{s_i/\mu_i}{V/\ell} \ll 1. \quad (4b)$$

Scaling up the detector size is critical to provide high detection efficiency and sensitivity. When operating the detector in the single-neutron counting mode, the equivalent noise charge in a

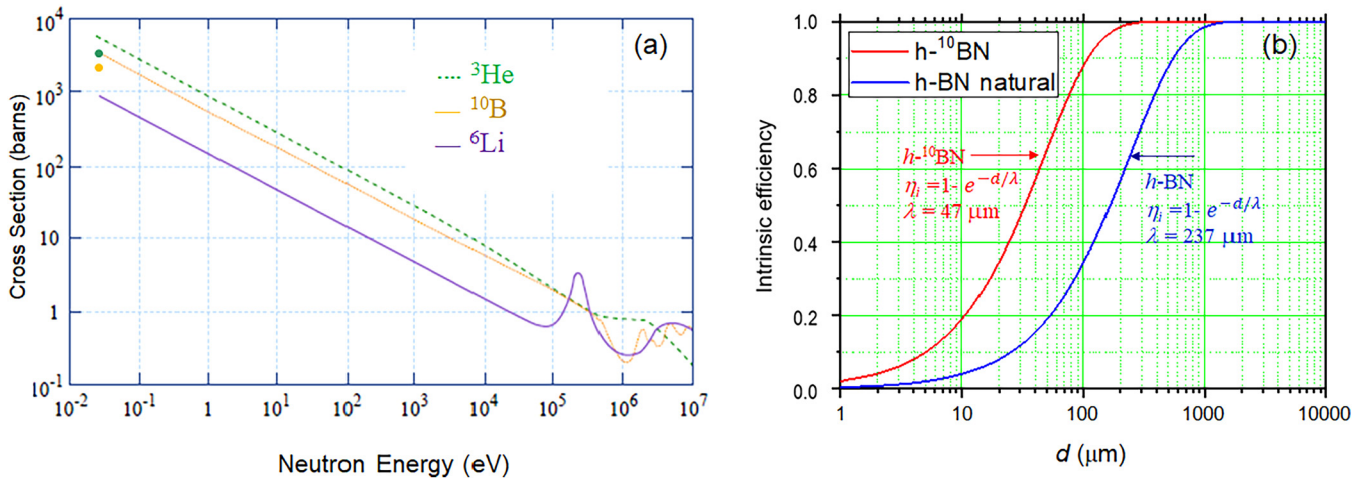


FIG. 5. (a) Neutron capture cross sections as functions of the kinetic energy of neutrons for ^3He , ^{10}B , and ^6Li . The green and orange dots indicate, respectively, the cross sections of ^3He and ^{10}B for thermal neutrons (neutrons with an average energy of 0.025 eV) (Credit: MIT OpenCourseWare, https://ocw.mit.edu/courses/nuclear-engineering/22-106-neutron-interactions-and-applications-spring-2010/lecture-notes/MIT22_106S10_lec07.pdf, Slide 27). (b) Plot of Eq. (3): The theoretical thermal neutron detection efficiency (η_i) as a function of the detector thickness (d) for 100% ^{10}B -enriched h-BN (h- ^{10}B N, red curve) and for natural h-BN (blue curve). λ denotes the thermal neutron absorption length.

02 May 2024 20:44:59

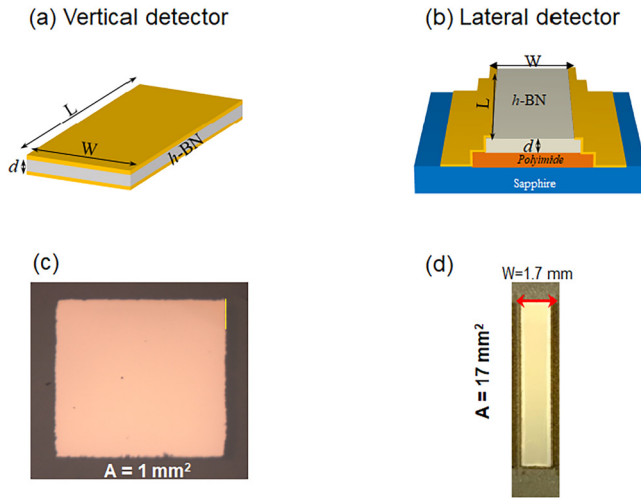


FIG. 6. Examples of h-BN neutron detectors. (a) A vertical detector, in which the applied field is V/d . (b) A lateral detector, in which the applied field is V/W . Schematics of the device geometry are illustrated in the top panel and examples of fabricated devices are shown in the bottom panel.

simple CR-RC shaper increases with the detector's dark current I_d and equivalent input capacitance (C).⁴⁷ Due to the nature of its UWBG, h-BN wafers are highly resistive ($>10^{13} \Omega \text{ cm}$) and the contribution from the detector's dark current to the equivalent noise is less of an issue. However, an increase in the capacitance and surface recombination while scaling up the device size needs to be addressed.

As shown schematically in Fig. 1(a), h-BN has a layered crystalline structure. As such, its physical properties are highly anisotropic with its carrier mobility in the c -plane (μ_a) being ~ 2 orders of magnitude larger than its mobility in the c -direction (μ_c).⁴⁷ This anisotropic behavior is also expected in other materials with a layered crystalline structure.⁴⁸ As illustrated in Fig. 6, in addition to the more traditional vertical detectors [Fig. 6(a)], we have also developed a lateral detector architecture [Fig. 6(b)] by taking advantages of h-BN's superior lateral transport properties.^{47,49} Table I compares the transport properties between a vertical detector in Fig. 6(a) and a lateral detector in Fig. 6(b). As can be seen from Table I, by fabricating the detector in a lateral geometry, for

detectors with the same dimension of 0.2 cm (width, W) \times 2.0 cm (length, L) \times $100 \mu\text{m}$ (thickness, d), the carrier mobility can be enhanced by nearly 2 orders of magnitude, the device capacitance can be reduced by a factor of 400 and the surface recombination field becomes negligibly small (reduced by a factor of 2000).

An "on-chip" integration processing scheme has been developed to fabricate large area detectors in a lateral geometry, as schematically illustrated in Fig. 7(a). The processing steps include to: (1) attach freestanding h-BN wafer to sapphire via highly insulating and adhesive polyimide coating; (2) perform laser dicing to obtain detector strips with a desired width and length, (3) design and fabricate metal mask by laser dicing according to the detector strip width and length, (4) perform metallization of a bi-layer of Ni/Au on the two edges of each detector strip using the metal mask, and (5) connect all detector strips in parallel to form a large area detector via an appropriate package. Optical image of a finished 1 cm^2 thermal neutron detector fabricated by combining 6 detector strips fabricated from a ^{10}B enrich h-BN ($h\text{-}^{10}\text{BN}$) quasi-bulk wafer ($100 \mu\text{m}$ thick) using this processing flow is shown in Fig. 7(b). It is worth noting that these multi-strip detectors differ from the traditional "interdigital finger" detectors with contacts typically fabricated on sample's top surface.³³ Each detector strip within the 1 cm^2 detector shown in Fig. 7(b) has a configuration of step-5 in Fig. 7(a) or Fig. 6(b), in which the metal contacts cover the entire vertical edges of the detector of $100 \mu\text{m}$ deep to ensure that the electric field is uniformly applied in the c -plane through the bulk of the detector material.

A Californium-252 (^{252}Cf) source from Frontier Technology was used as a neutron source. The number of neutrons as a function of energy of the ^{252}Cf fission source follows a mathematical function, the Watt function of $P(E) = 0.4865 (\sinh \sqrt{2E}) e^{-E} \text{ MeV}^{-1}$, with an average neutron energy of 2.13 MeV and the most probable neutron energy of 0.7 MeV .⁵⁰ A cube made of high-density polyethylene (HDPE) is used to moderate the fast neutrons via elastic scattering between neutrons and hydrogen atoms inside HDPE. Incoming fast neutrons from the ^{252}Cf source lose their energies after elastic scattering with hydrogen atoms. The neutron moderator setup used in this experiment was adopted from a previous work and is shown in Figs. 8(a) and 8(b).⁵¹ When the ^{252}Cf source is placed at position A (middle of the HDPE moderator), the probability of neutron emission reaching outside of the HDPE block is nearly zero. On the other hand, when the ^{252}Cf source is placed at 2.5 cm from the front surface of the HDPE block, i.e.,

02 May 2024 20:44:59

TABLE I. Lateral vs vertical detector geometry—Advantages of a lateral detector architecture revealed by comparing the transport properties between h-BN lateral detector and vertical detector. The illustration is for detectors with a dimension of 0.2 cm (width, W) \times 2.0 cm (length, L) \times $100 \mu\text{m}$ (thickness, d) assuming $\epsilon_a = \epsilon_c$, where μ_a and μ_c denote carrier mobilities in the c -plane (lateral) and in the c -direction (vertical), respectively; ϵ_a and ϵ_c denote static dielectric constants in the c -plane (lateral) and in the c -direction (vertical), respectively.

Quantity	Vertical	Lateral	Lateral/vertical	Lateral/vertical
Mobility lateral (μ_a) and vertical (μ_c)	μ_c	μ_a	μ_a/μ_c	~ 100
Capacitance (C)	$\epsilon_c(LW/d)$	$\epsilon_a(Ld/W)$	$(\epsilon_a/\epsilon_c)(d^2/W^2)$	$1/400$
Surface recombination velocity (s)	$\sim LW$	$\sim Ld$	d/W	$1/20$
Surface recombination field (s/μ)	$\sim LW/\mu_c$	$\sim Ld/\mu_a$	$(d/W)(\mu_c/\mu_a)$	$1/2000$
Applied electric field (E_a)	V/d	V/W	d/W	$1/20$

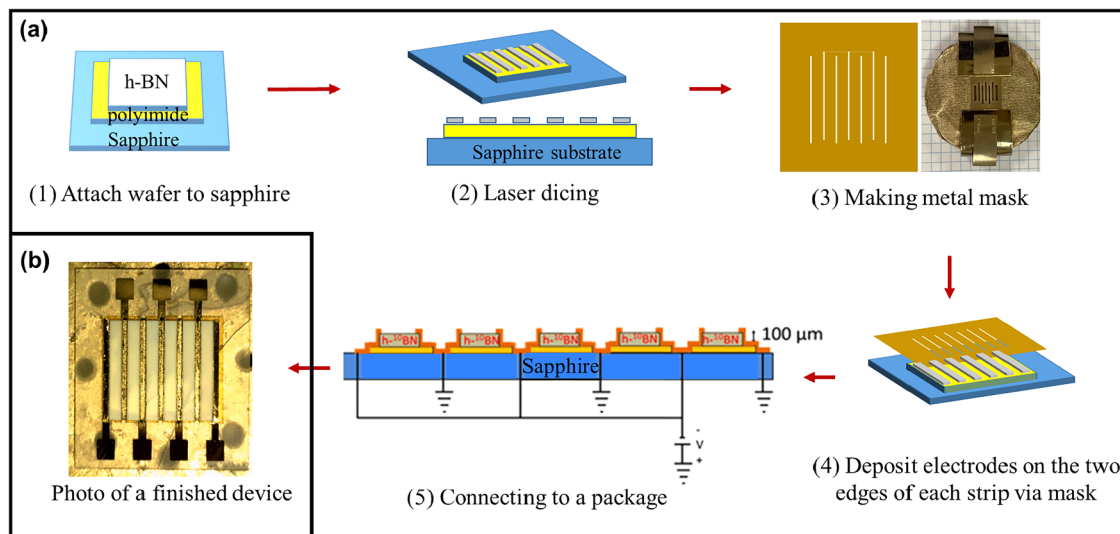


FIG. 7. (a) Processing flow for fabricating a large area lateral h-BN thermal neutron detector by combining multiple detector strips “on-chip.” (b) Optical image of a finished 1 cm^2 thermal neutron detector formed by connecting in parallel 6 detector strips fabricated from a $100\text{ }\mu\text{m}$ thick ^{10}B enrich h-BN ($\text{h-}^{10}\text{BN}$) wafer using this processing flow.

position B, a maximum flux of thermal neutrons is obtained.^{51–55} Detection electronics consist of a charge sensitive preamplifier, pulse shaping amplifier, and multichannel analyzer (Amtek MCA 8000D).^{54,55} The thermal neutron detection efficiencies were measured by placing the detectors at 30 cm from the HDPE block front

face and side-by-side with a ^6LiF filled micro-structured semiconductor neutron detector (MSND) with a known detection area (4 cm^2) and detection efficiency (30%) from Radiation Detection Technologies. By measuring the counts against that of MSND

02 May 2024 20:44:59

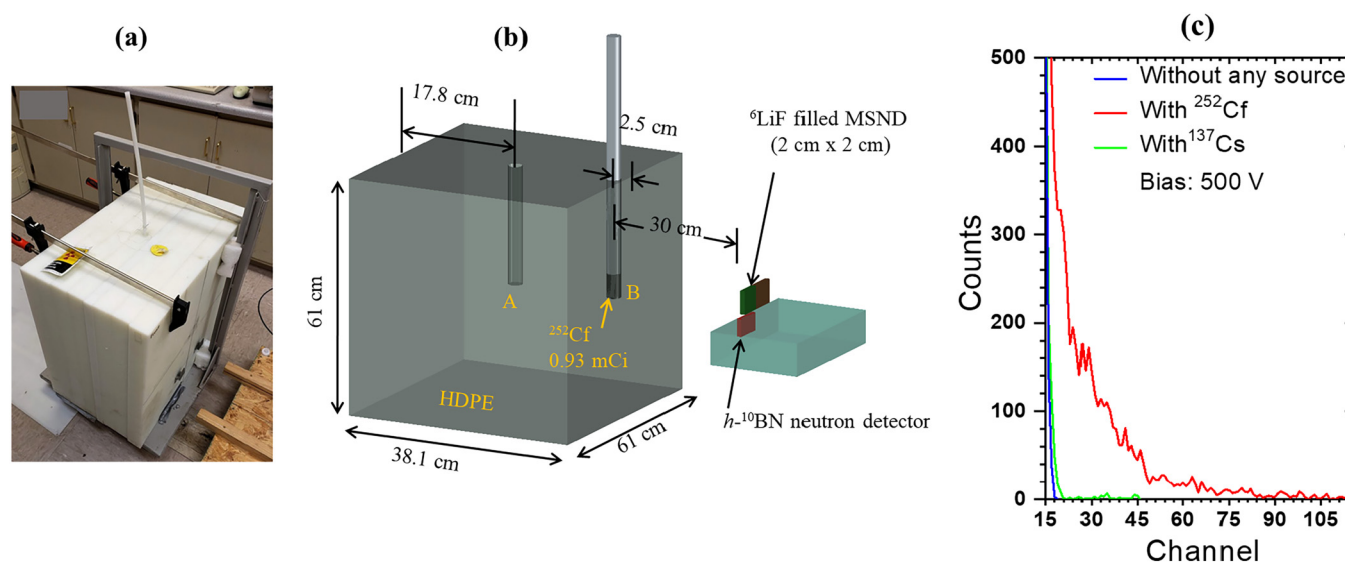


FIG. 8. (a) Photo of the thermal neutron source produced by ^{252}Cf in conjunction with a high-density-polyethylene (HDPE) moderator and (b) schematic diagram of experimental setup for characterizing the thermal neutron detection efficiencies of h-BN detectors. (c) Pulsed height spectra (PHS) of a representative $\text{h-}^{10}\text{BN}$ detector, in which the red curve is the response to thermal neutrons, the blue curve is the background (or dark) counts measured at the same bias voltage and the green curve is the response to gamma photons emitted from a ^{137}Cs source measured at the same bias voltage [reproduced from Fig. 3 of Ref. 49, Maity *et al.*, Appl. Phys. Lett. **116**, 142102 (2020). Copyright 2020 AIP Publishing LLC].

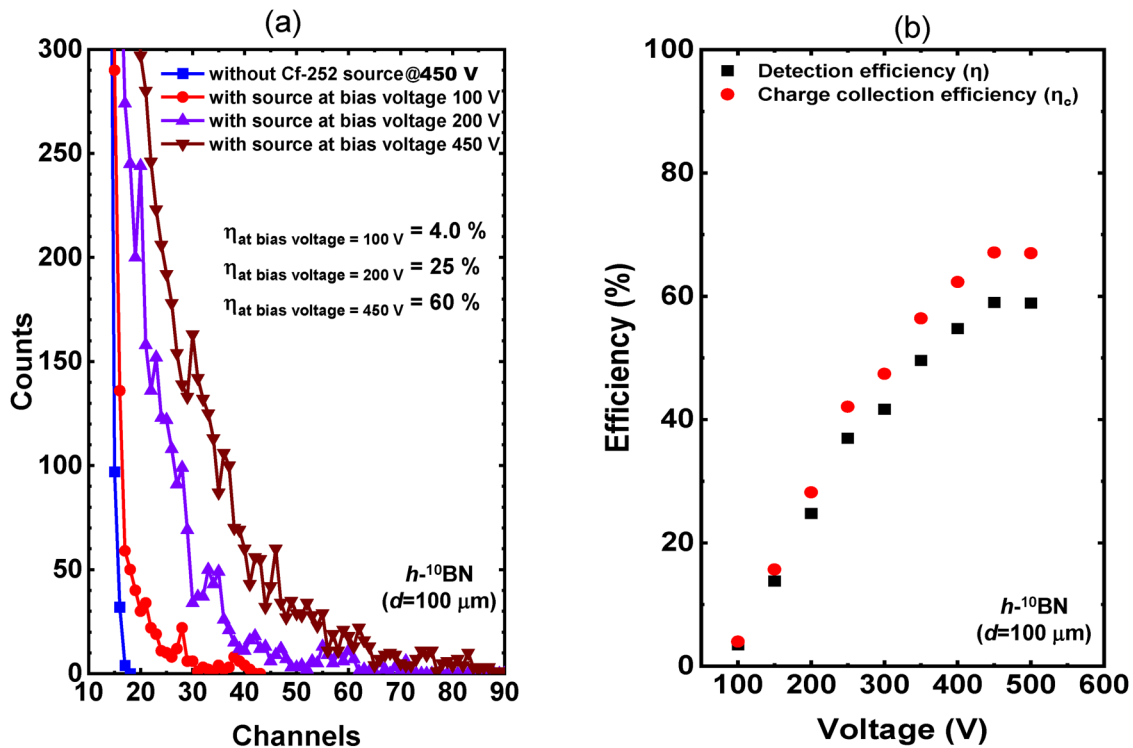


FIG. 9. (a) Pulse height spectra (PHS) measured at several representative applied voltages of a $1\ \text{cm}^2$ lateral detector fabricated from a $100\ \mu\text{m}$ thick ^{10}B -enriched $h\text{-}^{10}\text{BN}$ ($h\text{-}^{10}\text{BN}$) quasi-bulk wafer by connecting 6 lateral strips in parallel [Fig. 7(b)]. The red, purple, and brown curves are the responses to thermal neutrons with different bias voltages. The blue curve is the background (or dark) counts measured at a bias voltage of 450 V. (b) Plot of the measured detection efficiency (η) and effective charge collection efficiency (η_c) as functions of the applied voltage.

02 May 2024 20:44:59

obtained. The acquired pulsed height spectra (PHS) of a representative $h\text{-}^{10}\text{BN}$ detector are shown in Fig. 8(c), in which the red curve is the response to thermal neutrons, the blue curve is the background (or dark) counts measured at the same bias voltage and the green curve is the response to gamma photons emitted from a 662 keV ^{137}Cs source measured at the same bias voltage.

Figure 9 shows pulsed height spectra (PHS) of a $1\ \text{cm}^2$ lateral detector fabricated from a $100\ \mu\text{m}$ thick $h\text{-}^{10}\text{BN}$ wafer, measured at several representative bias voltages. By setting the lower-level discrimination (LLD) in the detection electronics corresponding to the response of the detector to 662 keV ^{137}Cs gamma photons as shown in Fig. 8(c), any response to gamma photons was successfully filtered out. This is because BN is composed of low atomic number elements B and N. However, as we further scale up devices to larger thicknesses, the responses to gamma photons of different energies need to be more carefully monitored. The measured detector efficiency (η) as a function of the applied voltage (and electric field) is plotted in Fig. 9(b), which shows that this $1\ \text{cm}^2$ detector delivers an overall detection efficiency of $\sim 60\%$ at a bias voltage of 450 V for thermal neutrons and that η saturates with further increasing the applied voltage. The measured detection efficiency presents the highest among all solid-state neutron detectors. By defining the effective charge collection efficiency (η_c) as the ratio of

the measured efficiency to the theoretical efficiency expressed by Eq. (3), $\eta_c (= \eta/\eta_i)$ as a function the applied voltage (and electric field) is plotted in Fig. 9(b), yielding a maximum charge collection efficiency of 68%. Based on the XRD and PL results, the presence of impurities and native defects plays a significant role in limiting the charge collection efficiency, as they can trap free carriers.⁴²

We also noted that the charge collection efficiency is nearly zero when the applied voltage is below 100 V. We believe this is caused by two factors. First, forming ohmic contacts to the as-grown $h\text{-}^{10}\text{BN}$ with a typical electrical resistivity of $\rho \sim 10^{13}\ \Omega\ \text{cm}$ is very challenging. The fabricated contacts are mostly blocking type which induces a surface barrier that needs to be overcome by applying a minimum electric field before a sizable charge collection by the electrodes can occur. Forming high-quality metal contacts, either ohmic or Schottky type, on UWBGs requires much more work. Secondly, it is well known that the exciton binding energy in $h\text{-}^{10}\text{BN}$ is exceptionally large, with reported values on the order of 100 s meV.^{56–60} The large exciton binding energy is expected to have a large impact on the performance of $h\text{-}^{10}\text{BN}$ neutron detectors, which rely on the processes of charge carrier collection with the aid of an applied electric field.

In both scenarios discussed above, the detection efficiency of $h\text{-}^{10}\text{BN}$ detectors is expected to enhance at higher temperatures. To

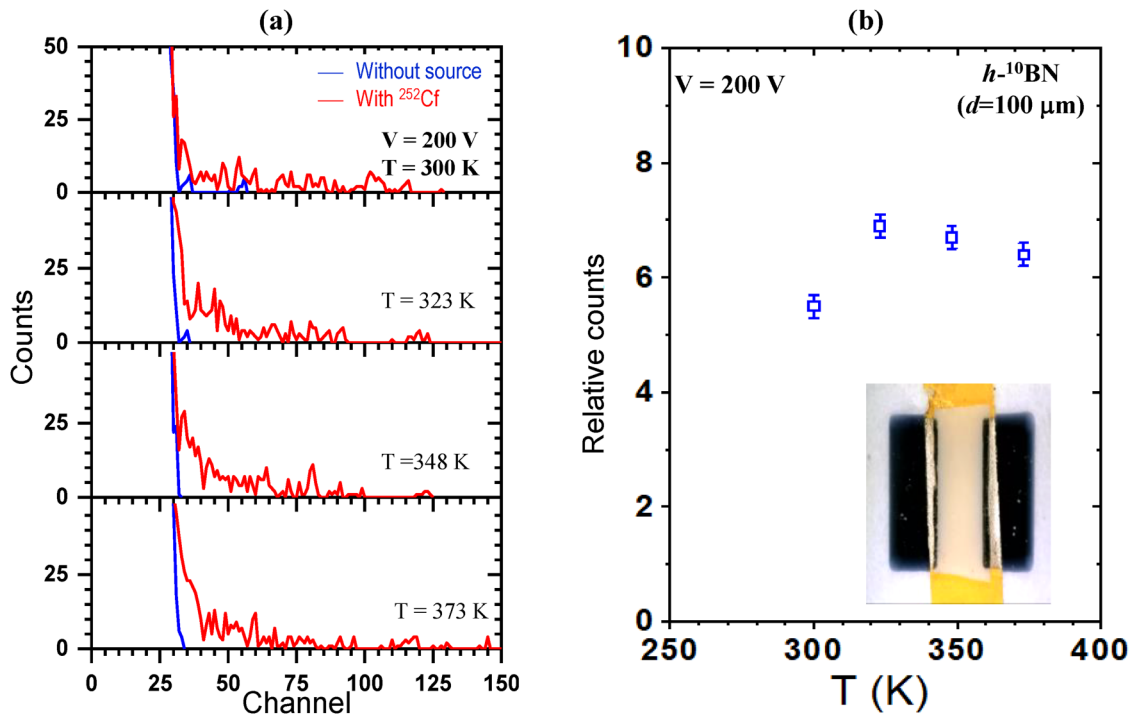


FIG. 10. (a) Pulse height spectra (PHS) of a $h\text{-}^{10}\text{BN}$ detector strip recorded at varying operating temperatures. The neutron responses (red curves) were recorded by placing the detector at 30 cm away from the ^{252}Cf source for 15 min, biased at 200 V. The blue curves are the background (or dark) counts measured at 200 V. (b) Plot of the relative thermal neutron counts detected by the detector strip vs the operating temperature. The inset is a micrograph of the detector used for the thermal neutron counts measurements at varying temperatures.

check this possibility, a single 1.7 mm wide detector strip was fabricated from a $100\ \mu\text{m}$ thick $h\text{-}^{10}\text{BN}$ wafer and used for the relative detection efficiency characterization at elevated temperatures by incorporating a resistive heater which provides an operating temperature up to $130\ \text{C}$. The relative thermal neutron detection efficiencies of this detector strip have been measured at varying operating temperatures and Fig. 10(a) shows the raw data of pulse height spectra (PHS) in response to thermal neutrons recorded at different temperatures at a bias voltage of 200 V. Figure 10(b) plots the relative thermal neutron counts vs detector’s temperature. The results of Fig. 10 demonstrated that the overall detection efficiencies at elevated temperatures are higher than the room temperature detection efficiency.

In a previous work, the key parameters which determine the charge collection efficiency (η_c) at varying temperatures have been examined.⁴³ These key parameters are defined by Many’s equation for describing the photocurrent-voltage (I-V) characteristics of a photoconductive detector described below,⁶¹

$$\eta_{c,i}(V) = \left[\frac{V\mu_i\tau_i \left(1 - e^{-\frac{W^2}{V\mu_i\tau_i}}\right)}{W^2 \left(1 + \frac{s_i W}{\mu_i V}\right)} \right]. \quad (i = e, h). \quad (5)$$

Here, $\mu_h\tau_h$ ($\mu_e\tau_e$) and s_h (s_e) define the mobility-lifetime product and surface recombination velocity for holes (electrons), respectively. V is the applied voltage between two electrodes of distance W (or $h\text{-}^{10}\text{BN}$ detector strip width), providing an applied electric field of $E_a = V/W$. The numerator and the denominator terms of Eq. (5) describe the charge collection efficiency limited by the bulk trapping effect (or $\mu\tau$ product) and ratio of surface recombination velocity to mobility (s/μ) or the “surface recombination field,” respectively.

By measuring the I-V characteristics under photoexcitation for the electron transport at different temperatures,⁴³ the $\mu\tau$ products and s/μ for electrons have been obtained by fitting the measured I-V characteristics shown in Fig. 11(a) with Eq. (5) and the results are shown in Figs. 11(b) and 11(c). Figure 11(b) shows that $\mu\tau$ increases with detector temperature up to 380 K, whereas Fig. 11(c) shows that s/μ continuously decreases with detector’s temperature. Inspecting Eq. (5), the dependencies of $\mu\tau$ and s/μ on temperature shown in Figs. 11(b) and 11(c) imply that the charge collection efficiencies at higher temperatures are enhanced over those at room temperatures, which further corroborate the results shown in Fig. 10. The enhancement of the charge collection efficiency at elevated temperatures can be accounted for by a thermal activation behavior of the surface electrons into the bulk⁴³ as well as possibly by the effect of enhanced exciton dissociation^{62–64} at

02 May 2024 20:44:59

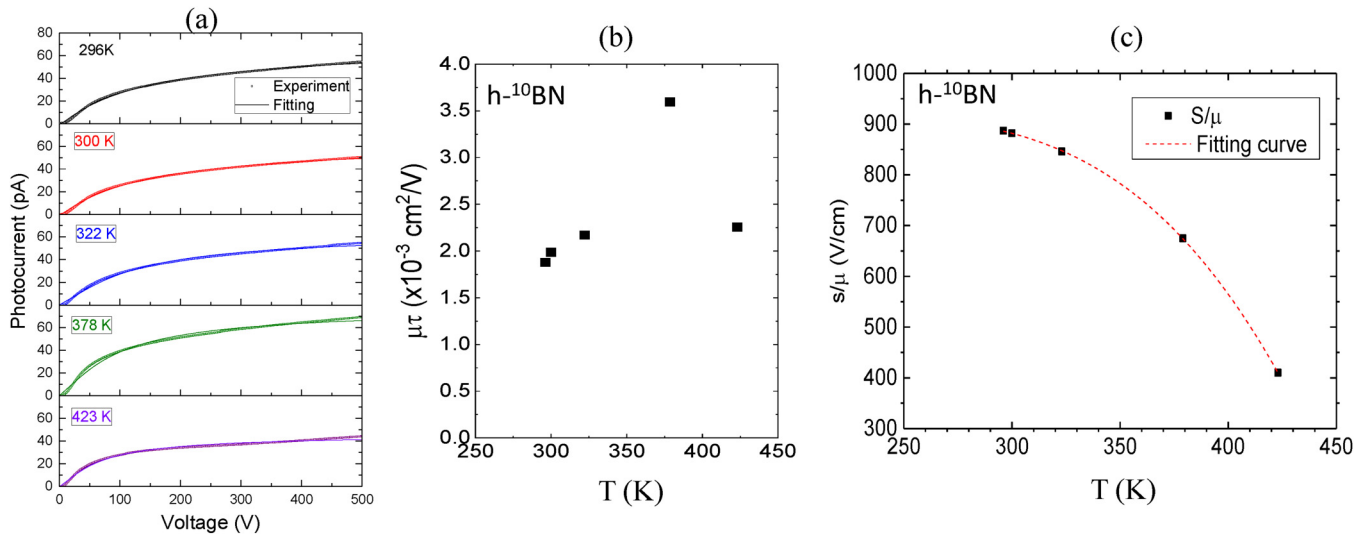


FIG. 11. (a) Photocurrent-voltage characteristics for electron transport. The solid curves are the least squares fitting using Eq. (5), from which the parameters of electron mobility-lifetime ($\mu\tau$) products and surface recombination field (s/μ or E_s) can be obtained at different temperatures. (b) Measured $\mu\tau$ as a function of temperature. (c) Measured surface recombination field (s/μ) as a function of temperature and the solid curve is the least squares fitting with $s/\mu = A[1 - \text{Bexp}(-T_0/T)]$. Light source used for photoexcitation was a broad-spectrum light source covering wavelength ranging between 170 and 2100 nm. Figures are reproduced with permission from Li *et al.*, Appl. Phys. Lett. **118**, 092102 (2021). Copyright 2021 AIP Publishing LLC.

higher temperatures. We believe that the results of detection efficiency enhancement at elevated temperatures shown in Figs. 10 and 11 are significant for applications of h-BN neutron detectors in areas of well logging, nuclear reactors monitoring and nuclear materials sensing, where temperatures can be substantially higher than 300 K.

III. SUMMARY

In summary, we provided an overview of the status of the crystal growth development of h-BN quasi-bulk wafers by HVPE. The crystalline and optical qualities of h-BN quasi-bulk crystals have been compared to those of the state-of-the-art bulk crystal flakes synthesized by the high-temperature/high-pressure (HT/HP) and by the metal flux solution method at atmospheric pressures. The results revealed that h-BN quasi-bulk crystals with a thickness around $100 \mu\text{m}$ have a good stacking sequence and long-range order in the *c* axis. However, the comparison results on optical properties clearly point out that optimizing the growth conditions to reduce the impurities such as oxygen and native defects is desired. The thermal neutron detector of 1 cm^2 in detection area fabricated from a $100 \mu\text{m}$ thick ^{10}B -enriched h-BN wafer was shown to deliver a detection efficiency of 60% at a bias voltage of 450 V. Moreover, the detection efficiency enhances at elevated temperatures, which is expected to be advantageous for applications of h-BN neutron detectors operating in high temperature and harsh environments, including in areas of well logging, nuclear reactors monitoring and nuclear materials sensing. The development of high efficiency h-BN neutron detector technology serves as a

stepstone for advancing the crystal growth technology to produce electronic grade h-BN quasi-bulk crystals.

ACKNOWLEDGMENTS

This research was supported by DOE ARPA-E (Nos. DE-AR0001257 and DE-AR0001552, monitored by Dr. Olga Spahn, Dr. Isik Kizilyalli, and Dr. Eric Carlson). Jiang and Lin are grateful to the AT&T Foundation for the support of Ed Whitacre and Linda Whitacre endowed chairs.

AUTHOR DECLARATIONS

Conflict of Interest

The authors have no conflict to disclose.

Author Contributions

Z. Alemoush: Data curation (equal); Formal analysis (equal); Investigation (equal); Methodology (equal); Software (equal); Validation (equal); Visualization (equal). **A. Tingsuwatit:** Data curation (equal); Formal analysis (equal); Investigation (equal); Methodology (equal); Validation (equal); Visualization (equal). **A. Maity:** Data curation (equal); Investigation (equal); Methodology (equal); Software (equal); Validation (equal); Visualization (equal); Writing – original draft (equal). **J. Li:** Data curation (equal); Formal analysis (equal); Investigation (equal); Methodology (equal); Software (equal); Supervision (equal); Validation (equal); Visualization (equal). **J. Y. Lin:** Conceptualization (equal); Formal analysis (equal); Funding acquisition (equal); Methodology (equal); Project administration

(equal); Resources (equal); Supervision (equal); Validation (equal); Visualization (equal); Writing – original draft (equal); Writing – review & editing (equal). **H. X. Jiang**: Conceptualization (equal); Formal analysis (equal); Funding acquisition (equal); Investigation (equal); Methodology (equal); Project administration (equal); Resources (equal); Supervision (equal); Validation (equal); Visualization (equal); Writing – review & editing (equal).

DATA AVAILABILITY

The data that support the findings of this study are available within the article.

REFERENCES

- ¹See <https://www.nobelprize.org/prizes/physics/2014/press-release/> for the Nobel Prize in Physics 2014.
- ²S. Nakamura, S. J. Pearson, and G. Fasol, *The Blue Laser Diode* (Springer, Berlin, 2000).
- ³H. X. Jiang and J. Y. Lin, *Nat. Electron.* **6**, 257 (2023).
- ⁴J. Wu, W. Walukiewicz, K. Yu, J. W. Ager III, E. E. Haller, H. Lu, W. J. Schaff, Y. Saito, and Y. Nanishi, *Appl. Phys. Lett.* **80**, 3967 (2022).
- ⁵H. Amano *et al.*, *J. Phys. D: Appl. Phys.* **51**, 163001 (2018).
- ⁶I. C. Kizilyalli, O. B. Spahn, and E. P. Carlson, *ECS Trans.* **109**, 3 (2022).
- ⁷M. S. Shur, in *SPIE Proceedings, Terahertz, RF, Millimeter, and Submillimeter-Wave Technology and Applications XVI*, 12420 (SPIE, 2023), p. 124200H.
- ⁸T. Sugino, K. Tanioka, S. Kawasaki, and J. Shirafuji, *Jpn. Appl. Phys.* **36**, L463 (1997).
- ⁹K. Watanabe, T. Taniguchi, and H. Kanda, *Nat. Mater.* **3**, 404 (2004).
- ¹⁰K. Watanabe, T. Taniguchi, and H. Kanda, *Nat. Photonics* **3**, 591 (2009).
- ¹¹H. X. Jiang and J. Y. Lin, *Semicond. Sci. Technol.* **29**, 084003 (2014).
- ¹²N. Alem, R. Erni, C. Kisielowski, M. D. Rossell, W. Gannett, and A. Zettl, *Phys. Rev. B* **80**, 155425 (2009).
- ¹³L. Song, L. Ci, H. Lu, P. B. Sorokin, C. Jin, J. Ni, A. G. Kvashnin, D. G. Kvashnin, J. Lou, B. I. Yakobson, and P. M. Ajayan, *Nano Lett.* **10**, 3209 (2010).
- ¹⁴R. V. Gorbachev, I. Riaz, R. R. Nair, R. Jalil, L. Britnell, B. D. Belle, E. W. Hill, K. S. Novoselov, K. Watanabe, T. Taniguchi, A. K. Geim, and P. Blake, *Small* **7**, 465 (2011).
- ¹⁵T. T. Tran, C. Elbadawi, D. Totonjian, C. J. Lobo, G. Grosso, H. Moon, D. R. Englund, M. J. Ford, I. Aharonovich, and M. Toth, *ACS Nano* **10**, 7331 (2016).
- ¹⁶N. R. Jungwirth, B. Calderon, Y. Ji, M. G. Spencer, M. E. Flatté, and G. D. Fuchs, *Nano Lett.* **16**, 6052 (2016).
- ¹⁷Z. Shotan, H. Jayakumar, C. R. Consideine, M. Mackoite, H. Fedder, J. Wrachtrup, A. Alkauskas, M. W. Doherty, V. M. Menon, and C. A. Meriles, *ACS Photonics* **3**, 2490 (2016).
- ¹⁸M. Kianinia, B. Regan, S. A. Tawfik, T. T. Tran, M. J. Ford, I. Aharonovich, and M. Toth, *ACS Photonics* **4**, 768 (2017).
- ¹⁹T. Ishii and T. Sato, *J. Cryst. Growth* **61**, 689 (1983).
- ²⁰T. Taniguchi and K. Watanabe, *J. Cryst. Growth* **303**, 525 (2007).
- ²¹N. D. Zhigadlo, *J. Cryst. Growth* **402**, 308 (2014).
- ²²J. Li, J. Wang, X. Zhang, C. Elias, G. Ye, D. Evans, G. Eda, J. M. Redwing, G. Cassabois, B. Gil, P. Valvin, R. He, B. Liu, and J. H. Edgar, *Chem. Mater.* **32**, 5066 (2020).
- ²³J. Li, X. K. Cao, T. B. Hoffman, J. H. Edgar, J. Y. Lin, and H. X. Jiang, *Appl. Phys. Lett.* **108**, 122101 (2016).
- ²⁴E. A. Preble, J. H. Leach, R. Metzger, E. Shishkin, and K. A. Udinary, *Phys. Status Solidi C* **11**, 604 (2014).
- ²⁵K. Yamane, Y. Hashimoto, H. Furuya, T. Inagaki, N. Okada, and K. Tadamoto, *Phys. Status Solidi C* **11**, 401 (2014).
- ²⁶Y. Kumagai, K. Goto, T. Nagashima, R. Yamamoto, M. Bockowski, and J. Kotani, *Appl. Phys. Express* **15**, 115501 (2022).
- ²⁷S. Kaneki, T. Konno, T. Kimura, K. Kanegae, J. Suda, and H. Fujikura, *Appl. Phys. Lett.* **124**, 012105 (2024).
- ²⁸K. Ohnishi, N. Fujimoto, S. Nitta, H. Watanabe, S. Lu, M. Deki, Y. Honda, and H. Amano, *J. Appl. Phys.* **132**, 145703 (2022).
- ²⁹Z. Alemoush, N. K. Hossain, A. Tingsuwatit, M. Almohammad, J. Li, J. Y. Lin, and H. X. Jiang, *Appl. Phys. Lett.* **122**, 012105 (2023).
- ³⁰Z. Alemoush, A. Tingsuwatit, J. Li, J. Y. Lin, and H. X. Jiang, *Crystals* **13**, 1319 (2023).
- ³¹R. S. Pease, *Acta Cryst.* **5**, 356 (1952).
- ³²A. Maity, S. J. Grenadier, J. Li, J. Y. Lin, and H. X. Jiang, *Prog. Quantum Electron.* **76**, 100302 (2021).
- ³³J. Li, R. Dahal, S. Majety, J. Y. Lin, and H. X. Jiang, *Nuclear Inst. Methods Phys. Res. Sect. A* **654**, 417 (2011).
- ³⁴K. Ahmed, R. Dahal, A. Weltz, J.-Q. Lu, Y. Danon, and I. B. Bhat, *Appl. Phys. Lett.* **109**, 113501 (2016).
- ³⁵X. Yang, S. Nitta, K. Nagamatsu, S. Y. Bae, H. J. Lee, Y. H. Liu, M. Pristovsek, Y. Honda, and H. Amano, *J. Cryst. Growth* **482**, 1 (2018).
- ³⁶A. Mballo, A. Ahaitouf, S. Sundaram, A. Srivastava, V. Ottapilakkal, R. Gujrati, P. Vuong, S. Karrakchou, M. Kumar, X. Li, Y. Halfaya, S. Gautier, P. L. Voss, J. P. Salvestrini, and A. Ougazzaden, *ACS Omega* **7**, 804 (2022).
- ³⁷G. Siegel, G. Gryzbowcki, A. Hilton, C. Muratore, and M. Snure, *Crystal* **9**, 339 (2019).
- ³⁸X. Z. Du, J. Li, J. Y. Lin, and H. X. Jiang, *Appl. Phys. Lett.* **108**, 052106 (2016).
- ³⁹K. Watanabe and T. Taniguchi, *Phys. Rev. B* **79**, 193104 (2009).
- ⁴⁰S. J. Grenadier, A. Maity, J. Li, J. Y. Lin, and H. X. Jiang, *Appl. Phys. Lett.* **112**, 162103 (2018).
- ⁴¹M. Almohammad, Z. Alemoush, J. Li, J. Y. Lin, and H. X. Jiang, *Appl. Phys. Lett.* **124**, 102106 (2024).
- ⁴²L. Weston, D. Wickramaratne, M. Mackoite, A. Alkauskas, and C. G. Van de Walle, *Phys. Rev. B* **97**, 214104 (2018).
- ⁴³J. Li, A. Maity, S. J. Grenadier, J. Y. Lin, and H. X. Jiang, *Appl. Phys. Lett.* **118**, 092102 (2021).
- ⁴⁴A. Tingsuwatit, A. Maity, S. J. Grenadier, J. Li, J. Y. Lin, and H. X. Jiang, *Appl. Phys. Lett.* **120**, 232103 (2022).
- ⁴⁵O. Osberghaus, *Z. Phys.* **128**, 366 (1950).
- ⁴⁶G. F. Knoll, *Radiation Detection and Measurement*, 4th ed. (John Wiley & Sons, 2010).
- ⁴⁷A. Maity, S. J. Grenadier, J. Li, J. Y. Lin, and H. X. Jiang, *Appl. Phys. Lett.* **114**, 222102 (2019).
- ⁴⁸Y. K. Chung, J. Lee, W. G. Lee, D. Sung, S. Chae, S. Oh, K. H. Choi, B. J. Kim, J. Y. Choi, and J. Huh, *ACS Omega* **6**, 26782 (2021).
- ⁴⁹A. Maity, S. J. Grenadier, J. Li, J. Y. Lin, and H. X. Jiang, *Appl. Phys. Lett.* **116**, 142102 (2020).
- ⁵⁰F. H. Frohner, *Nucl. Sci. Eng.* **106**, 345 (1990).
- ⁵¹J. Clinton, “Optimization and characterization of a novel self powered solid state neutron detector,” Ph.D. thesis (Rensselaer Polytechnic Institute, 2011).
- ⁵²W. A. Noonan, “Neutrons: It is all in the timing—The physics of nuclear fission chains and their detection,” *Johns Hopkins Apl.: Technical Digest* **32**, 762 (2014).
- ⁵³T. C. Doan, “Thermal neutron detector based on hexagonal boron nitride,” Ph.D. thesis (Texas Tech University, 2016).
- ⁵⁴A. Maity, “Highly sensitive hexagonal boron nitride thermal neutron detectors,” Ph.D. thesis (Texas Tech University, 2020).
- ⁵⁵S. J. Grenadier, “Advancements in hexagonal boron nitride for thermal neutron detection applications,” Ph.D. thesis (Texas Tech University, 2020).
- ⁵⁶B. Arnaud, S. Lebigue, P. Rabiller, and M. Alouani, *Phys. Rev. Lett.* **96**, 026402 (2006); **100**, 189702 (2008).
- ⁵⁷L. Wirtz, A. Marini, and A. Rubio, *Phys. Rev. Lett.* **96**, 126104 (2006).

⁵⁸K. Watanabe and T. Taniguchi, *Int. J. Appl. Ceram. Technol.* **8**, 977 (2011).

⁵⁹L. Museur, G. Brasse, A. Pierret, S. Maine, B. Attal-Tretout, F. Ducastelle, A. Loiseau, J. Barjon, K. Watanabe, T. Taniguchi, and A. Kanaev, *Phys. Status Solidi (RRL)* **5**, 214 (2011).

⁶⁰G. Cassabois, P. Valvin, and B. Gil, *Nat. Photonics* **10**, 262 (2016).

⁶¹A. Many, *J. Phys. Chem. Solids* **26**, 575 (1965).

⁶²H. C. Kamban and T. G. Pedersen, *Phys. Rev. B* **100**, 045307 (2019).

⁶³S. Hastrup, S. Latini, K. Bolotin, and K. S. Thygesen, *Phys. Rev. B* **94**, 041401 (2016).

⁶⁴H. C. Kamban and T. G. Pedersen, *Sci. Rep.* **10**, 5537 (2020).